# Colloidal Gelation in Liquid Metals Enables Functional Nanocomposites of 2D Metal Carbides (MXenes) and Lightweight Metals

Vladislav Kamysbayev,[†] Nicole M. James,[†] Alexander S. Filatov,[†] Vishwas Srivastava,[†] Babak Anasori,[‡ϖ] Heinrich M. Jaeger,[⊥] Yury Gogotsi,[‡] and Dmitri V. Talapin[†§*]

[†]*Department of Chemistry and James Franck Institute, University of Chicago, Chicago, IL 60637, United States*

[‡]*A. J. Drexel Nanomaterials Institute and Department of Materials Science and Engineering, Drexel University, Philadelphia, PA 19104, United States*

[⊥]*Department of Physics and James Franck Institute, University of Chicago, Chicago, IL 60637, United States*

[§]*Center for Nanoscale Materials, Argonne National Laboratory, Argonne, IL 60439, United States*

[ϖ]*Current address: Integrated Nanosystems Development Institute, Department of Mechanical and Energy Engineering, Purdue School of Engineering and Technology, Indiana University–Purdue University Indianapolis, Indianapolis, IN 46202, United States*

*E-mail: dvtalapin@uchicago.edu

## ABSTRACT

Nanomaterials dispersed in different media, such as liquids or polymers, generate a variety of functional composites with synergistic properties. In this work we discuss liquid metals as the

This is the author's manuscript of the article published in final edited form as:

Kamysbayev, V., James, N. M., Filatov, A. S., Srivastava, V., Anasori, B., Jaeger, H. M., … Talapin, D. V. (2019). Colloidal Gelation in Liquid Metals Enables Functional Nanocomposites of 2D Metal Carbides (MXenes) and Lightweight Metals. ACS Nano. https://doi.org/10.1021/acsnano.9b06207

nanomaterials' dispersion media. For example, 2D transition metal carbides and nitrides (MXenes) can be efficiently dispersed in liquid Ga and lightweight alloys of Al, Mg, Li. We show that the Lifshitz theory predicts strong van der Waals attraction between nanoscale objects interacting through liquid metals. However, a uniform distribution of MXenes in liquid metals can be achieved through colloidal gelation, where particles form self-supporting networks stable against macroscopic phase segregation. This network acts as a reinforcement boosting mechanical properties of the resulting metal-matrix composite. By choosing Mg-Li alloy as an example of ultra-lightweight metal matrix and $Ti_3C_2T_x$ MXene as a nanoscale reinforcement, we apply liquid metal gelation technique to fabricate functional nanocomposites with up to 57 % increase in the specific yield strength without compromising the matrix alloy's plasticity. MXenes largely retain their phase and 2D morphology after processing in liquid Mg-Li alloy at 700 °C. The 2D morphology enables formation of a strong semi-coherent interface between MXene and metal matrix, manifested by biaxial strain of the MXene lattice inside the metal matrix. This work expands applications for MXenes and shows the potential for developing MXene-reinforced metal matrix composites for structural alloys and other emerging applications with metal-MXene interfaces, such as batteries and supercapacitors.

**KEYWORDS**: liquid metals, van der Waals attraction, colloidal gel, lightweight alloys, MXenes

Composites of nanostructures embedded in a second phase (matrix) enable emerging functionalities due to strong coupling between optical, electronic and mechanical properties.[1] Nanostructures in glasses and polymers have found applications in smart windows,[2] electromagnetic interference shielding[3] and energy storage.[4] Metallurgists combine nanostructures with metals to prepare metal-matrix composites (MMCs) with enhanced mechanical properties. Particle-reinforced MMCs are an important class of composite materials consisting of lightweight elements (Al, Mg, Li) as the metal matrix and ceramic particle reinforcements. Properties of the soft metal matrix, such as yield strength, fatigue, and corrosion resistance, can be significantly improved with the addition of hard ceramic nanostructures.[5] Commercially available ceramic and carbon nanostructures such as SiC,[6] $Al_2O_3$,[7] graphene platelets,[8] and carbon nanotubes,[9] have been integrated into metals *via* powder metallurgy techniques, usually resulting in weak interfacial bonding between the metal matrix and the nano-inclusions.[5] As an alternative to the powder

metallurgy methods, direct dispersion of nanostructures in liquid metals for fabricating MMCs has several advantages, such as stronger bonding between the components[10,11] and greater compatibility with large scale manufacturing.[12] However aggregation and subsequent macroscopic phase segregation of particles in liquid metals presents a major challenge in achieving uniform MMCs.

In addition, given the high reactivity of molten Al, Mg, and Li at elevated temperatures, the choice of nanostructures suitable for MMC fabrication is limited to materials stable in these media. Carbon-deficient early transition metal carbides (such as $TiC_y$, $y < 1$) are stable in molten Mg and Li across a broad range of temperatures.[13] Unfortunately, these metal carbide particles show a strong tendency toward aggregation in metal matrices,[14] preventing their uniform distribution in MMCs. Here, we discuss the peculiarities of liquid metals as the particle dispersion media and introduce a promising class of MMCs utilizing 2D metal carbide nanostructures (MXenes).

MXenes are a large class of 2D metal carbides and nitrides, which have metal-terminated surfaces with tunable surface chemistry.[15] MXenes have a formula unit of $M_{n+1}X_nT_x$ ($n$ = 1-3), where M represents an early transition metal (Ti, Mo, V, Nb, W *etc*.), X is carbon or nitrogen, and $T_x$ represents surface functionalities (–F, –OH, =O).[16] $Ti_3C_2T_x$, the most studied MXene today, has a thickness of ~1 nm and hexagonal close-packed (hcp) structure (Figure 1a) with a Ti terminated (0001) surface, thus potentially providing means of bonding with the metal matrix, directly or *via* surface oxygen atoms. Strong covalent bonding between in-plane Ti and C atoms is responsible for MXenes' excellent mechanical properties. The experimentally measured 2D Young modulus of an individual $Ti_3C_2T_x$ sheet is 326±29 N/m (corresponding to 330±30 GPa bulk modulus), which is the highest among solution processable 2D materials.[17] The calculated bending rigidity of 49.6 eV[18] far exceeds that of graphene (1.2 eV)[19] and other classes of 2D materials due to the greater thickness (~1 nm) of an individual MXene sheet. The combination of metal terminated surfaces, strong in-plane bonding and excellent mechanical properties make $Ti_3C_2T_x$ attractive reinforcements for lightweight MMCs.

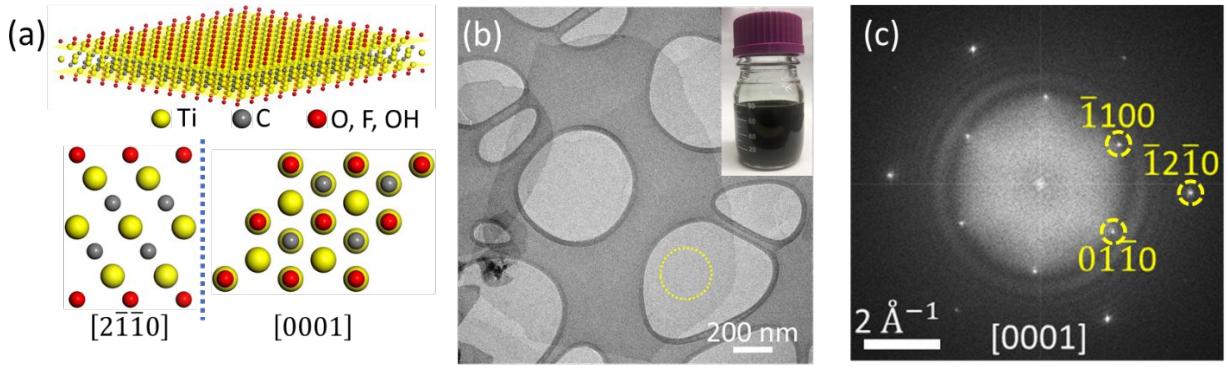


**Figure 1.** (a) Structure of the monolayer $Ti_3C_2T_x$; (b) TEM image of a $Ti_3C_2T_x$ flake deposited from the colloidal solution on a lacey carbon grid (inset: photograph of the colloidal solution of 2D MXene sheets in water). (c) FFT of the circled region in panel (b) showing single-crystallinity and hexagonal symmetry of the individual flake.

In this work, we first develop a general method for achieving a uniform distribution of MXenes in liquid metals by creating a colloidal gel. In this gelled state, the particles are able to form self-supporting networks, which are stable against macroscopic phase segregation. By using a Mg-Li alloy as an example of an ultra-lightweight structural alloy,[20] we further demonstrate the successful integration of 2D $Ti_3C_2T_x$ flakes in Mg-Li alloy *via* the liquid metal gelation route. The $Ti_3C_2T_x$ flakes retain their 2D morphology after processing in molten Mg-Li alloy in the form of $Ti_3C_2$ nanoplatelets (NPLs). The composites show a uniform distribution of $Ti_3C_2$ NPLs and enhanced specific yield strength over the neat metal alloy while fully retaining the base metal's plasticity. Interestingly, the 2D $Ti_3C_2$ NPLs experience biaxial strain while inside the metal matrix. This biaxial straining is attributed to the formation of a strong semi-coherent interface between the NPLs and metal matrix.

## RESULTS AND DISCUSSION

**Preparation and exfoliation of MXene sheets.** Exfoliated MXene sheets were synthesized following an established procedure.[21] Briefly, $Ti_3C_2T_x$ sheets were obtained from the corresponding $Ti_3AlC_2$ MAX phase *via* simultaneous etching of Al and intercalation with $Li^+$ ions in LiF/HCl solution. The final product of this process is a colloidal solution of single- to few-flake

$Ti_3C_2T_x$ MXene (Figure 1b). Fast Fourier transform (FFT) analysis of a representative transmission electron microscopy (TEM) image (Figure 1c) shows a hexagonal pattern corresponding to the [0001] zone axis of the single-crystal $Ti_3C_2T_x$ structure. Atomic force microscopy (AFM) confirms the presence of monolayer MXene flakes with a thickness of 1.5 nm (Figure S1). Thickness of a single flake of $Ti_3C_2T_x$ MXene is ~1 nm. The larger measured thickness in AFM is due to the presence of water molecules between MXene and the substrate.[17]

The $Li^+$ intercalated MXene powder was further treated with aqueous tetramethylammonium hydroxide (TMAOH) to substitute the $Li^+$ ions for $TMA^+$ ions. This substitution increased the center-to-center interlayer spacing in MXene films from 10.9 Å to 14.6 Å (Figure S2). The resulting increased interlayer spacing was found to be advantageous for the subsequent liquid metal infiltration in between MXene sheets. In addition to increasing the interlayer spacing, the TMAOH treatment results in MXenes with reduced lateral dimensions (Figure S3)[22] which is also advantageous for fabricating uniform MMCs due to the reduced van der Waals (vdW) attraction between the smaller MXene flakes. TMAOH adsorbed on $Ti_3C_2T_x$ surface decomposes cleanly forming gaseous $NH_2/NH_3/NH_4^+$ and $CO/CO_2$ at above 300 °C and hence does not leave any organic residue behind.[23] The $TMA^+$ intercalated $Ti_3C_2T_x$ flakes were used throughout this study, unless stated otherwise.

**Liquid metals as particle dispersion media.** One of the challenges for dispersing nanostructures directly into a liquid metal is poor wetting of ceramic surfaces by liquid metals.[24] From a thermodynamic point of view, NCs are wetted by liquids when the work of adhesion between the liquid and the NC surface ($-W_{ad}$) exceeds the liquid-vapor surface tension ($\sigma_{LV}$). This wetting condition can be easily satisfied in the case of traditional solvents, such as water at 25 °C with $\sigma_{LV}$ of 0.072 J/m$^2$. However, this condition becomes more severe in the case of liquid metals, such as liquid Al at 660 °C (melting point) with $\sigma_{LV}$ of 0.871 J/m$^2$.[25] Adhesion energy on the order of 1 J/m$^2$ between a liquid metal and ceramic surface can be achieved through direct chemical bonding.[26] However, the chemical reaction at the interface should not compromise the phase or structure of the ceramic NCs. The Ti rich facets of carbon deficient $TiC_y$ ($y < 1$) are known to exhibit enhanced wettability by liquid metals compared to the mixed atom (C and Ti)-terminated surfaces. This is related to the stronger liquid metal-Ti interfacial bonding when the surface Ti atoms have fewer C neighbors.[27]

From a colloidal science perspective, particles disperse uniformly in liquids if the repulsive terms dominate the long-range interparticle potentials. Typically, the repulsive forces have a steric or electrostatic origin while the attractive interactions come from vdW forces.[28] However, due to perfect polarizability, liquid metals efficiently screen the electrostatic potential immediately next to the NC surface, suggesting that classical electrostatic double layer repulsion is not possible. Moreover, the absence of solvated long chain ligands at the NC surfaces eliminates the possibility of steric stabilization. In analogy with NCs in molten inorganic salts,[29] the chemical affinity of the liquid metal to a ceramic surface can, in principle, induce liquid metal restructuring[30-32] leading to oscillatory solvation interactions. However, this mode of interaction is expected to be short ranged (~0.5 nm) in liquid metals and can be both attractive and repulsive between planar surfaces.[33]

The vdW interaction potential *V(l)* for two parallel $Ti_3C_2T_x$ sheets at sub-10 nm distances (*l*), where the retardation effects can be ignored, can be written as:[34]

$$V(l) = -\frac{A}{12\pi}\left(\frac{1}{l^2} - \frac{2}{(l+b)^2} + \frac{1}{(l+2b)^2}\right)\cdot Area\,,$$

where *A* is a Hamaker coefficient and *b* is the thickness of a MXene sheet (~1 nm). To assess the attractive potential acting on the particles dispersed in a liquid metal, we used the Lifshitz theory, which expresses the Hamaker coefficient through the complex dielectric functions of the particles and the medium between them. Since the Lifshitz theory does not rely on pairwise additivity of the individual intermolecular forces,[34] it allows for an accurate estimation of the vdW force acting on particles immersed in highly conductive media, such as liquid metals. Using the experimental spectroscopic ellipsometry data for $Ti_3C_2T_x$,[35] we reconstructed the complex dielectric function and calculated Hamaker coefficients (see Supporting Information for details). Table 1 summarizes the calculated Hamaker coefficients for the three systems of interest: $Ti_3C_2T_x$ interacting through vacuum, $Ti_3C_2T_x$ interacting through liquid Ga, which is a typical example of liquid metal, and liquid Ga interacting through vacuum. If the Hamaker coefficient of $Ti_3C_2T_x$ in Ga were to be evaluated from the commonly used combining relation,[36] we would arrive at $A = \left(\sqrt{345} - \sqrt{381}\right)^2 = 0.89$ zJ. Clearly the combining relation breaks down when computing Hamaker coefficients for particles interacting through a liquid metal medium. This breakdown of the combining relations in liquid metals can be related to their large dielectric constant.[28] This

result demonstrates that the previously used[10, 36] combining relations for the approximation of the vdW attraction between nanoparticles interacting through a liquid metal medium underestimate the Hamaker coefficient and, correspondingly, the vdW attraction, by almost two orders of magnitude.

**Table 1.** Hamaker coefficients for $Ti_3C_2T_x$ and liquid Ga (vac stands for vacuum).

| System | $Ti_3C_2T_x$-vac-$Ti_3C_2T_x$ | Ga-vac-Ga | $Ti_3C_2T_x$-Ga-$Ti_3C_2T_x$ |
|---|---|---|---|
| A [zJ] | 381 | 345 | 50.4 |

Figure 2a shows the vdW potential between two MXene sheets with surface area of $100^2$ nm$^2$ in a liquid metal at 700 °C (temperature relevant for processing Mg-Li and other lightweight metal alloys) as a function of *l*. The vdW attraction exceeds the thermal energy of 86 meV up to ~8 nm of separation. This suggests that, in the absence of long-ranged repulsive forces, dispersions of $100^2$ nm$^2$ MXene sheets in liquid metals will spontaneously aggregate. Even much smaller $10^2$ nm$^2$ MXene flakes are expected to aggregate (Figure 2b). A qualitatively similar behavior is also predicted for spherical $TiC_{0.9}$ NCs dispersed in liquid metal (Figure 2b): the vdW interactions are too strong to permit the formation of stable colloidal solutions in the absence of long-ranged repulsive interactions. Although change in the $T_x$ composition in harsh liquid metal environment (Figure S9-10) can affect the complex dielectric function of MXenes,[37] the fact that the Hamaker coefficient for $TiC_{0.9}$-Ga-$TiC_{0.9}$ system (39.1 zJ, see Supporting Inofrmation for details) is close to that of $Ti_3C_2T_x$-Ga-$Ti_3C_2T_x$ suggests the $T_x$ compositon likely plays secondary role in determining the strenght of the vdW potential in liquid metals.

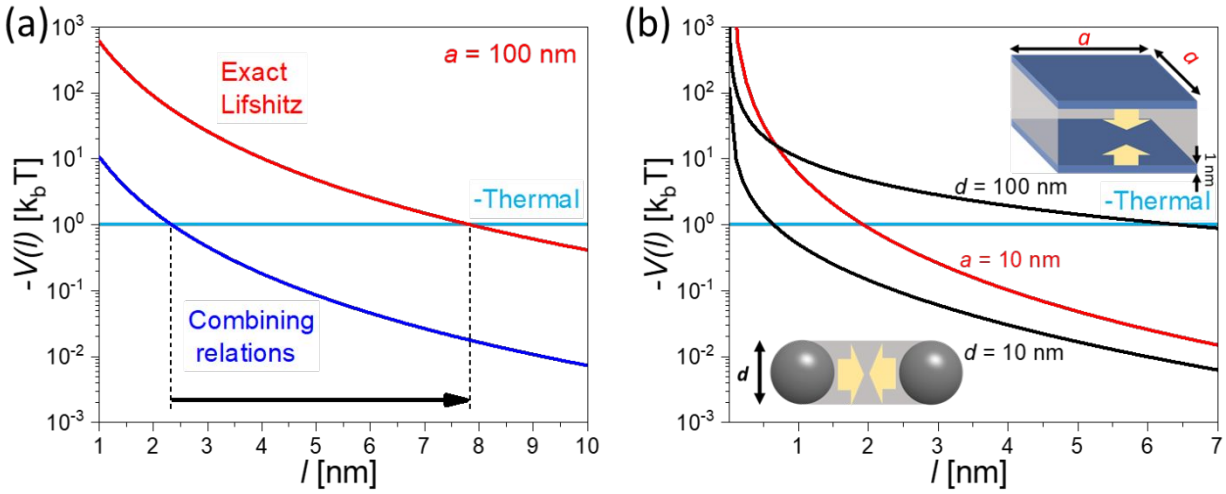


**Figure 2.** (a) vdW potential calculated using combining relations and exact Lifshitz approach for the two MXene sheets of lateral dimension *a* interacting through liquid Ga at 700 °C. (b) vdW potential calculated using exact Lifshitz approach for small-area MXene sheets and spherical $TiC_{0.9}$ NCs of diameter *d* interacting through liquid Ga at 700 °C.

**Colloidal gelation in liquid metals.** The strong vdW attraction and lack of long-range repulsive potentials suggest that ceramic particles, including MXene flakes, are not colloidally stable in a liquid metal environment. An alternative approach to prevent macroscopic phase segregation and achieve homogenous distribution of attractive inclusions in a metal is through the dynamic arrest of particles based on colloidal gelation.[38] In a colloidal gel, the volume-spanning network of particles can be stable against settling/creaming under gravity.[39] Such mechanically stable colloidal gels often form when the volume fraction of particles in a solution is high enough to reach a percolation threshold, *i.e.* allow formation of an infinite spanning cluster.[40]

The possibility of colloidal gelation in liquid metals can be probed directly by measuring the composite's viscoelastic properties. The linear viscoelastic storage ($G'$) and loss ($G''$) moduli determine the response of the system to a small oscillatory shear strain $\gamma = \gamma_0 \sin(\omega t)$ with amplitude $\gamma_0$ and frequency $\omega$ (Figure 3b). The stress follows as $\sigma = \sigma_0 \sin(\omega t + \delta)$, and the complex modulus of the material $G^* = G' + iG''$ has the storage and loss components determined as $G' = \frac{\gamma_0}{\sigma_0}\cos\delta$ and $G'' = \frac{\gamma_0}{\sigma_0}\sin\delta$. $G'$ gives insight into how a system stores the applied stress, and hence it determines the rigidity and connectivity of the particle network (if any) in the suspension.

$G''$ measures how system dissipates the applied stress. In an elastic material, $G' \gg G''$ while for a viscous fluid $G' = 0$.

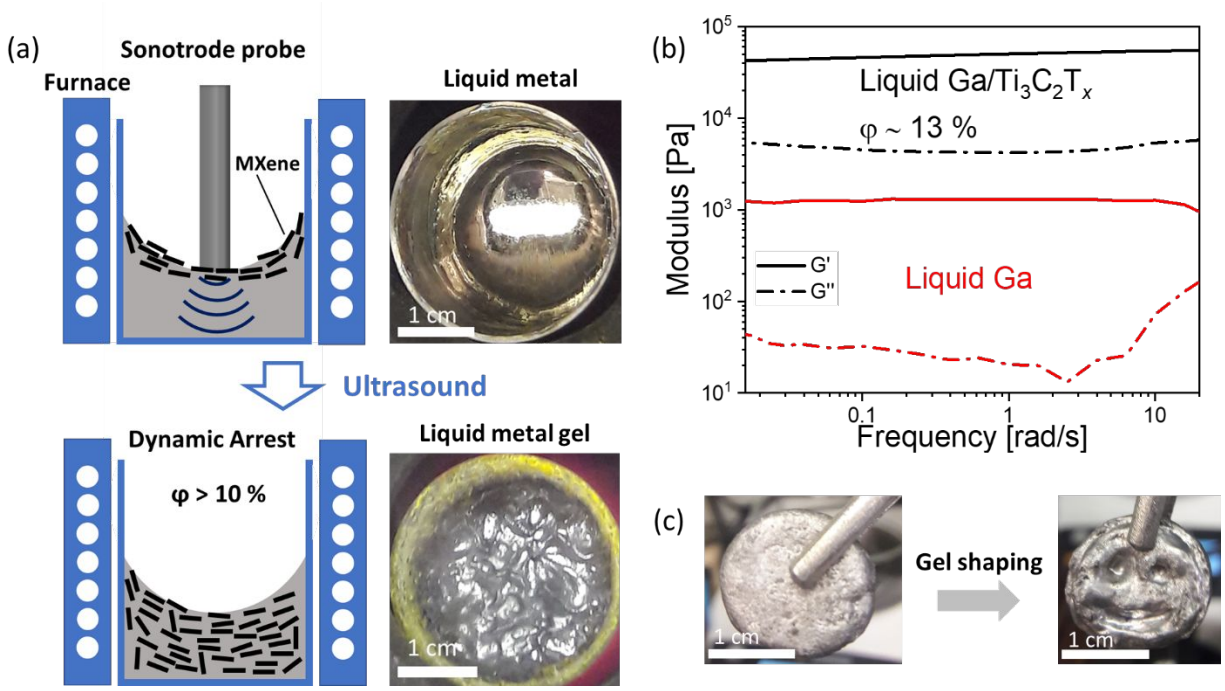


**Figure 3.** (a) Schematic for the preparation of $Ti_3C_2T_x$ MXene dispersions in lightweight metals and photographs of the crucibles. (b) Real (G') and imaginary (G") components of the complex modulus describing viscoelastic properties of liquid Ga with and without $Ti_3C_2T_x$ MXene flakes. (c) Demonstration of shaping the gelated composite of $Ti_3C_2T_x$ MXene in Al-Mg alloy (Figure S8) above the alloy melting temperature of 432 °C.

For rheological investigations, we used liquid Ga as a model system to determine conditions that can cause liquid metal gelation through the addition of $Ti_3C_2T_x$ MXene flakes. Ga has a melting point of 29.8 °C and surface tension of 0.711 J/m$^2$, thus it is a convenient near room temperature analog of the high melting point Mg-Li alloy discussed in the following sections.[41] The concentration of $Ti_3C_2T_x$ was built up in liquid Ga iteratively at 45 °C, as shown in Figure 3a, with the final concentration of $Ti_3C_2T_x$ sheets in liquid Ga set at ~13 vol. %. Figure 3b shows the frequency dependence of $G'$ and $G''$ in the linear viscoelastic regime at $\gamma_0$ = 0.05 % for the dispersion of $Ti_3C_2T_x$ in liquid Ga. Since $\gamma_0$ is small, it only weakly perturbs the equilibrium structure of the suspension (Figure S4).[42] Both $G'$ and $G''$ for the $Ti_3C_2T_x$ flakes suspensions are at

least 50 times larger than the corresponding moduli measured for liquid Ga coated with a thin layer of native oxide (Figure 3b, see Supporting Information for further discussion). Therefore, we attribute the observed viscoelastic properties of the composite to the presence of MXene flakes and treat the oxide layer effect as a weak perturbation. The composite's shear moduli are nearly frequency independent with $G' > G''$ across the measured frequency range. This is consistent with the formation of a colloidal gel.[43] The gel structure weakens progressively with time by applying steady shear in one direction (Figure S5) suggesting thixotropic behavior, which is also characteristic of gel networks.[44]

The observed aggregation and gelation phenomena for MXene flakes in liquid Ga can be used to predict the behavior of ceramic particles dispersed in liquid metals. At low volume fractions, aggregation of nanoflakes results in a macroscopic phase separation of $Ti_3C_2T_x$ in Ga (Figure S6), while at high volume fractions we observed the formation of extended particle networks. A qualitatively similar behavior was observed for $Ti_3C_2T_x$ in Mg-Li (discussed in the following sections) and $TiC_{0.9}$ microparticles (Figure S7) in Al-Mg alloys. In all cases, high particle loading was necessary to achieve a uniform distribution of particles. In addition to rendering uniform composites, the extended particle networks provided sufficient rigidity to shape metals directly in their molten state (Figure 3c). In a conventional semi-solid casting, viscoelastic properties of metal slurries are controlled through the volume fraction of the *in situ* nucleated precipitates in the region between solidus and liquidus lines in the equilibrium phase diagram.[45] However, two major limitations of this technique are: (i) it requires careful control over the temperature gradients which are difficult to realize on a large scale; (ii) alloys have to be of a certain composition. Since in our case the liquid metal viscoelastic moduli can be controlled independently through the formation of ceramic particles' networks, the lightweight metal alloys of an arbitrary chemical composition can become amenable to 3D printing above their thermodynamic melting points.[46]

**MXene/Mg-Li composite.** As a case study relevant to lightweight MMCs, we further explored $Ti_3C_2T_x$ dispersed in molten and solidified Mg-Li alloy (39 at. % Li). Mg-Li alloys containing more than 30 at. % of Li are the lightest known structural alloys currently investigated for aerospace and other applications. They crystalize in the body centered cubic (bcc) structure which significantly improves their room temperature ductility and corrosion resistance compared to that of Mg alloys with the hcp structure.[20] The combination of low density and good mechanical

properties make bcc Mg-Li alloys an interesting platform to study the effect of ceramic particles on their structural and mechanical properties. Informed by the rheological studies of MXenes in liquid Ga, the concentration of flakes was built up until the liquid Mg-Li alloy exhibited noticeable gel-like viscoelastic behavior, and was able to hold its shape against gravity (Figure 3a). Based on the X-ray fluorescence (XRF) elemental analysis (Mg:Ti = 4.2:1), we estimate that the volume fraction of $Ti_3C_2T_x$ MXene in the Mg-Li alloy is ~13%, similar to the volume fraction of the same MXenes in liquid Ga. TEM image (Figure 4a) and energy dispersive X-ray (EDX) elemental mapping (Figure 4b) of the composite show the formation of uniform particle networks consistent with the observation of a colloidal gel in liquid Ga composite containing a similar concentration of particles (Figure 3b). A high magnification TEM image (Figure 4c) suggests the presence of individual $Ti_3C_2$ flakes (dark contrast particles) forming a continuous network.

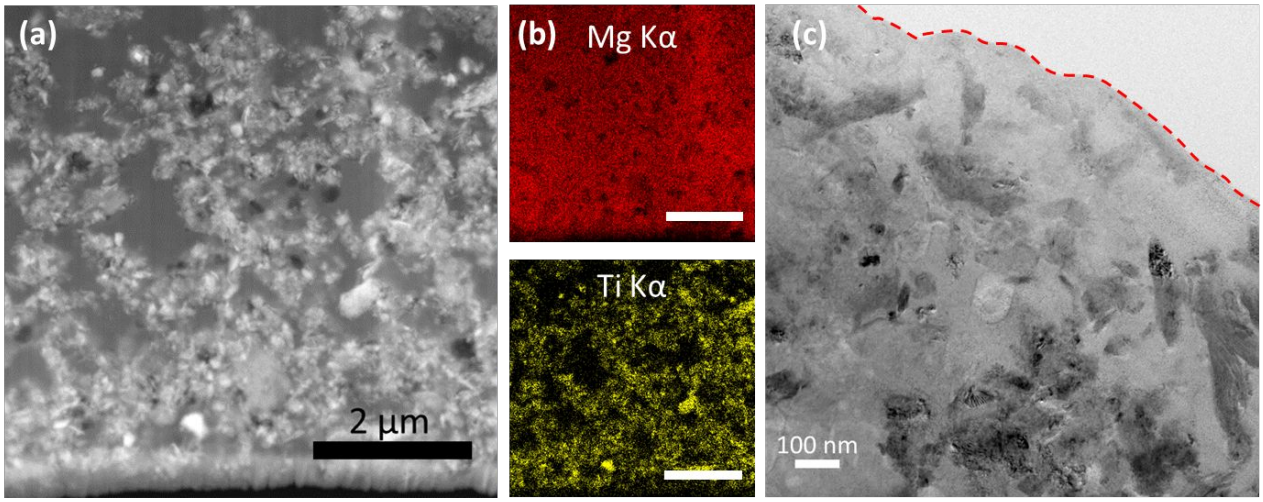


**Figure 4.** Electron microscopy characterization of $Ti_3C_2$ NPLs in Mg-Li alloy. (a) Large area dark-field TEM image showing particle network on the several micron scale. (b) Mg Kα and Ti Kα EDX elemental maps of the area shown in (a). (c) Bright field TEM image showing particle network on the submicron scale (dashed red line shows the sample's edge).

In order to check the stability of $Ti_3C_2T_x$ flakes at 700 ºC in the molten alloy, we assessed the crystalline phase, morphology, and surface functionalization of the materials recovered from the MXene/Mg-Li MMC by dissolving the metal matrix in aqueous HCl solution. X-ray photoelectron spectroscopy (XPS) spectra (Figures S9, S10 and Supporting Discussion) indicate that the

stoichiometry of the recovered particles is $Ti_3C_{2.2}$ (for simplicity we further refer to it as $Ti_3C_2$.). Additionally, XPS spectra show that the liquid metal treatment at 700 °C eliminated the fluoride surface groups and reduced the Ti oxidation state (Figure S9) suggesting the presence of bare $Ti_3C_2$ particles in Mg-Li alloy matrix. The Raman spectrum (Figure S11) of the recovered particles does not show peaks corresponding to $TiO_2$ or amorphous carbon, supporting the stability of titanium carbide phase under our processing conditions. The TEM images of the recovered $Ti_3C_2$ particles show NPLs with smaller lateral dimensions than the original 2D MXene sheets (Figure S12). AFM measurements confirm that the recovered particles retain their 2D morphology, though the thickness increases slightly to ~3 nm (Figure S13). An FFT of the TEM image of an individual NPL shows a hexagonal pattern consistent with the [0001] zone axis of the hcp structure (Figure S14). These results are consistent with a reported *in situ* TEM study where hcp-$Ti_3C_2T_x$ flakes heated above 500 °C grew thicker at the expense of their lateral area, while still preserving hexagonally symmetric Ti-terminated (0001) top and bottom facets.[47] In general, high-temperature stability of $Ti_3C_2T_x$ in molten Mg-Li is encouraging for making a variety of other MMCs by combining different MXenes with various metal matrices.

To better understand the role of particle shape, we compared MMCs prepared using 2D $Ti_3C_2T_x$ MXenes with similarly prepared MMCs containing isotropic $TiC_{0.9}$ NCs (Figure S15). The $TiC_{0.9}$ NCs with an average crystalline size of ~58 nm were introduced into Mg-Li alloy with a final atomic ratio of Mg:Ti of 4:1 (measured with XRF) corresponding to ~12 vol. % $TiC_{0.9}$ phase. Figure 5a shows high-resolution synchrotron XRD patterns for the pristine $Ti_3C_2T_x$ MXene powder, recovered $Ti_3C_2$ NPLs, and recovered isotropic $TiC_{0.9}$ NCs for comparison. The most intense wide-angle peak of the pristine $Ti_3C_2T_x$ corresponds to the diffraction from $(11\bar{2}0)$ planes, whereas their $(10\bar{1}0)$ peak overlaps strongly with the lamellar $(000L)$ and $(10\bar{1}L)$ reflections.[48] Based on the Rietveld refinement (Figure S16), the recovered $TiC_{0.9}$ NCs did not change their original isotropic rock-salt (fcc) structure. In contrast, the diffraction pattern of the recovered $Ti_3C_2$ NPLs differs from the original $Ti_3C_2T_x$ MXene phase and qualitatively resembles the recovered isotropic $TiC_{0.9}$ NC phase. However, Rietveld refinement using the pure isotropic fcc structure resulted in poor fitting, with the weighted-profile *R*-factor ($R_{wp}$) exceeding 10 % (Figure S17a). The fitting was significantly improved after introducing a secondary hcp phase and [110] texture for the fcc structure (Figure S17b). The synchrotron XRD results are thus in agreement with the FFT analysis of the high-resolution-TEM images (Figure S14): the recovered NPLs have increased

thickness (~3 nm) compared to the original $Ti_3C_2T_x$ (~1 nm) and their structure is a mixture of the hcp (37 %) and [110] textured fcc (63 %) phases.

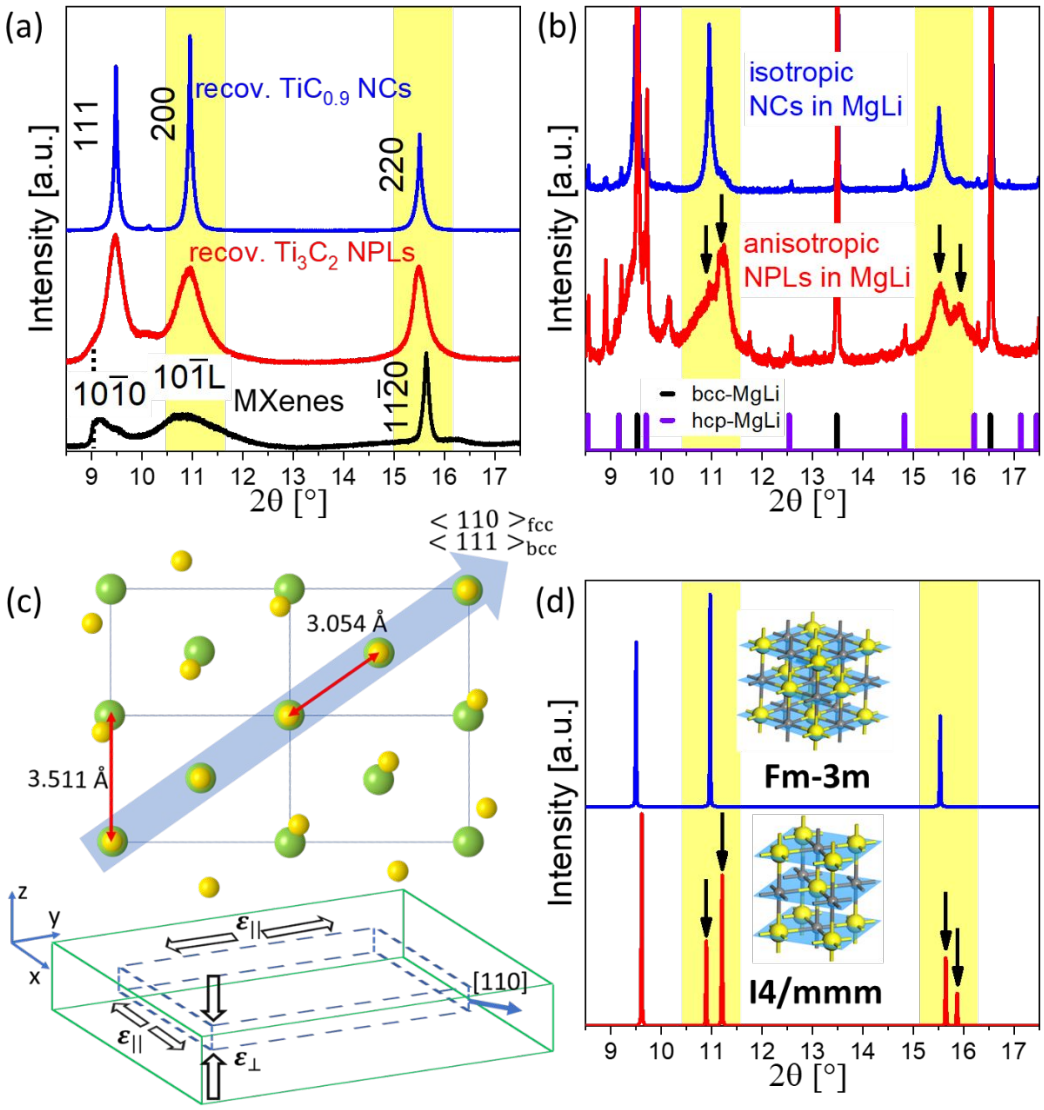


**Figure 5.** (a) Synchrotron XRD (λ = 0.412779 Å) patterns of the initial $Ti_3C_2T_x$ flakes intercalated with $TMA^+$ cations (black), flakes recovered from Mg-Li alloy (red) and isotropic $TiC_{0.9}$ NCs recovered from Mg-Li alloy (blue). (b) Synchrotron XRD patterns of the two Mg-Li MMCs containing $Ti_3C_2$ NPLs (red) and isotropic $TiC_{0.9}$ NCs (blue). (c) Schematic showing the biaxial strain observed in $Ti_3C_2$ NPLs embedded in Mg-Li matrix due to the Kudjumov-Sachs orientation relationship between (110) plane of bcc-MgLi alloy (green) and (111) Ti-terminated plane of fcc-$Ti_3C_2$ NPL (yellow). (d) Simulated XRD patterns for TiC in $Fm\bar{3}m$ and $I4/mmm$ space groups.

Next, we compared the synchrotron XRD patterns of $Ti_3C_2$ NPLs and $TiC_{0.9}$ NCs dispersed in solidified Mg-Li alloy matrix (Figure 5b). In both cases the solidified metal matrix consisted of the bcc-MgLi and hcp-MgLi as the major and minor phases, respectively (Figure S18).[20, 49] The regions highlighted in yellow correspond to diffraction from the planes of the titanium carbide phase that do not overlap with the strong matrix peaks. The (200) and (220) peaks of the $TiC_{0.9}$ NCs in the Mg-Li matrix are almost identical in their shape and peak position to the peaks of the recovered particles. However, $Ti_3C_2$ NPLs have a markedly different diffraction pattern while embedded in the matrix compared to their diffraction pattern after removal from the matrix: for the composite sample, the two peaks corresponding to the fcc structure, (200) at 10.95° 2-theta and (220) at 15.50°, each split into two peaks (Figure 5b). To further investigate this peak splitting, we used different Mg-Li alloys as the metal matrices and observed similar features in all studied MMCs containing $Ti_3C_2$ NPLs (Figure S19). The observed symmetry reduction of the $Ti_3C_2$ NPLs in Mg-Li alloy is consistent with a tetragonal distortion to the $I4/mmm$ space group, which is a maximal subgroup of the $Fm\bar{3}m$ space group[50] (Figure 5d). Since the recovered $Ti_3C_2$ NPLs lack the (200) and (220) peak splitting (Figure 5a, red curve), the tetragonal distortion cannot be attributed to alloying between Mg/Li and Ti. Instead, it may suggest that static strain imposed by the surrounding metal matrix is responsible for the NPL lattice distortion. The amount of the in-plane ($\varepsilon_{||}$) and out-of-plane ($\varepsilon_{\perp}$) strain is 0.72 % (tensile) and -2.09 % (compressive) (Figure 5c) respectively (see Supporting Information for details), which corresponds to a Poisson ratio (ν) of 0.34 for $Ti_3C_2$ NPLs and is in good agreement with the modelled ν of 0.31 for $Ti_3C_2(OH)_2$.[51]

The observed biaxial straining can originate from the formation of a semi-coherent interface between the matrix and $Ti_3C_2$ NPLs. Due to the small difference between nearest neighbors' distances in (111) plane of the fcc component of $Ti_3C_2$ NPLs, 3.054 Å, and in (110) plane of bcc-MgLi alloy, 3.041 Å, we hypothesize existence of $\{111\}<110>_{\mathrm{fcc-Ti_3C_2\,NPL}}||\{110\}<111>_{\mathrm{bcc-MgLi}}$ orientation relationship, known as the Kurdjumov-Sachs (KS) orientation (Figure 5c).[52] Similarly, the KS orientation can take place between (0001) plane of the hcp component of $Ti_3C_2$ NPLs (nearest neighbor distance of 2.927 Å) and (110) plane of bcc-MgLi alloy.

The biaxial straining of $Ti_3C_2$ NPLs inside the metal matrix is a direct consequence of their 2D morphology. $TiC_{0.9}$ NCs, on the other hand, are isotropic particles and hence they can only

experience hydrostatic strain inside the metal matrix. However, this strain is confined to the metal-NC interface and cannot significantly perturb the internal structure of $TiC_{0.9}$ NCs.

The biaxial strain observed in the $Ti_3C_2$ NPLs in Mg-Li alloy reflects strong bonding of the NPLs with the metal matrix, which has important implications on the mechanical performance of these MMCs. The MMC fabricated from $Ti_3C_2T_x$ MXenes shows a 128 % increase in the yield strength and a 57 % increase in the specific yield strength over the base Mg-Li alloy (Figure 6a and Table S1). This MMC is able to bear a gradually increasing load smoothly without any signs of crack formation. Additionally, reproducible results were obtained for the replicate samples, suggesting uniform distribution of particles (Figure S20a). The MMC fabricated with the isotropic $TiC_{0.9}$ NCs is also able to bear the load smoothly without signs of crack formation (Figure S20b). However, this MMC shows only a moderate increase in the yield strength (71 % for best sample) and specific yield strength (17 % for best sample) (Table S1). This difference in the mechanical performance may be explained by differences at the interfaces due to the interactions between the nanomaterials' surfaces and the metal matrix. The density functional theory (DFT) calculated work of adhesion ($-W_{ad}$) between the metal and ceramic interfaces is larger for polar ceramic facets.[53] Due to the KS orientation relationship between $Ti_3C_2$ NPLs and Mg-Li alloy, $Ti_3C_2$ NPLs maximize the area of polar $(111)_{fcc}$ and $(0001)_{hcp}$ facets per volume of particles in contact with the metal matrix. $TiC_{0.9}$ NCs, on the other hand, have non-polar facets (Figure S15) interfacing the metal matrix. Stronger chemical bonding at the interface, in turn, explains increased load transfer from the matrix to $Ti_3C_2$ NPLs compared to isotropic $TiC_{0.9}$ NCs. As discussed above, two-dimensional $Ti_3C_2$ NPLs elastically strain inside metal matrix to minimize lattice mismatch at the interface and, correspondingly, maximize the number of chemical bonds per unit area of the NPL-matrix interface.

The MMCs with the isotropic $TiC_{0.9}$ NCs did not yield reproducible results unlike the MMC with $Ti_3C_2$ (Figure S20). This can be attributed to the non-uniform distribution of NCs. The volume fraction required to achieve colloidal gelation with attractive isotropic particles is higher than that of attractive anisotropic particles. Our observations are thus qualitatively consistent with the phase diagram for patchy colloids, where colloids with a smaller number of nearest neighbor contacts (such as $Ti_3C_2$ NPLs) reach gelation and bypass phase segregation at lower volume fractions.[54]

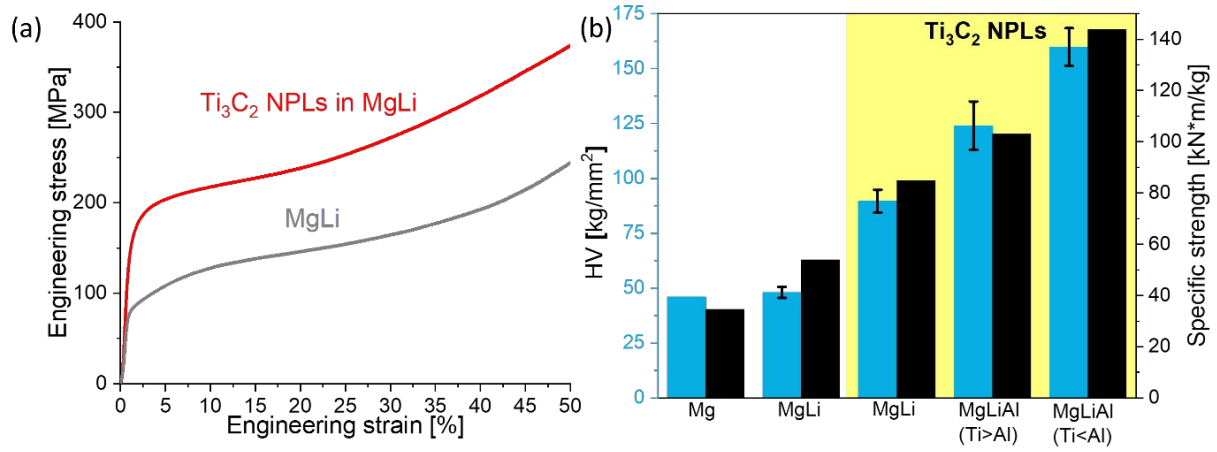


**Figure 6.** (a) Compressive engineering stress-strain curves for the Mg-Li alloy MMCs containing $Ti_3C_2$ NPLs (red) and Mg-Li alloy without any particles (grey). (b) Summary of the specific yield strength and Vickers hardness for the composites of $Ti_3C_2$ NPLs in Mg-Li and Mg-Li-Al alloys. The literature reported specific strength and Vickers hardness for pure Mg are shown for comparison.[55-56]

We further tested the effect of Al addition on the $Ti_3C_2$ in Mg-Li MMC. Al is commonly used in small amounts to strengthen Mg-Li alloys[20] and improve the wetting of TiC particles in Mg alloys.[57] Figure 6b shows the dependence of the specific yield strength and Vickers hardness (HV) at 0.98 N load for the $Ti_3C_2$ NPLs in Mg-Li MMCs with different amounts of added Al. With an elemental ratio of Ti to Al of 2.4/1 (measured with XRF), Al did not form any intermetallic compounds with Mg and Li (Figure S19), suggesting that Al preferentially interacts with the NPL surface. EDX elemental mapping of a thinned sample (Figure S21) further suggests segregation of the majority of the added Al to the $Ti_3C_2$ NPL-metal interface. In this case the specific strength increased by 91 % and hardness by 158 % over the base Mg-Li alloy. This increase in the strength is accompanied by the broadening of the (0002) reflection possibly suggesting that the addition of Al improves wetting of the individual $Ti_3C_2$ layers (Figure S19b). However, the composite could reach a maximum plastic strain of only 22 % before the first crack reached the surface of the specimen (Figure S22), showing more brittle behavior than the no-Al Mg-Li composites. Although Al was effective in increasing the strength of the composite without the formation of intermetallic phases, further optimization is required to improve the composite's plasticity. The introduction of Al at an atomic ratio exceeding that of Ti resulted in the formation of an AlLi intermetallic phase (Figure S19a, Figure S23), which additionally increased the strength at the expense of the alloy's

plasticity with the maximum plastic strain reaching only 9.7 % (Figure S22). This initial study shows the potential for developing MXene-reinforced MMCs with greatly improved mechanical properties. It is natural to assume that optimization of MXene content, particle size, dispersion and alloy composition will further improve the mechanical properties.

## CONCLUSIONS

This work demonstrates promising application for 2D MXenes as a reinforcement component for lightweight structural alloys. Uniform composites of lightweight metals and 2D MXenes have been enabled by the colloidal gelation of liquid metals. $Ti_3C_2T_x$ forms a network of $Ti_3C_2$ nanoplatelets spanning the volume of Mg-Li alloy matrix. The network formation is believed to be responsible for the lack of particle phase segregation while in the molten state and during melt solidification. The Mg-Li alloy shows increased load transfer to $Ti_3C_2$ nanoplatelets compared to isotropic $TiC_{0.9}$ nanocrystals due to the favorable orientation relationship between the basal plane of $Ti_3C_2$ NPLs and the (110) plane of bcc-MgLi, introducing biaxial straining in $Ti_3C_2$. This leads to the 128% increase in the yield strength of the alloy. By adding Al, one can further improve the mechanical properties of the composite. The specific strength and hardness almost tripled compared to the neat Mg-Li alloy. These numbers for a particular combination of MXene and a metal alloy are probably far from the maximum values possible for MXene-based metal matrix composites. We believe that the developed method for achieving uniform metal-matrix composites, based on the colloidal gelation of liquid metals, can be extended to other metal alloy-MXene systems. While we can assume that $Ti_2C$, $Ti_3CN$, $Ti_4N_3$ and other Ti-terminated MXenes will behave similarly to $Ti_3C_2$, MXenes based on other transition metals should be investigated. In particular, $Zr_3C_2$ MXene has been shown to retain its 2D lattice and morphology better than $Ti_3C_2$ MXene at high temperatures.[58] As a result, $Zr_3C_2$ MXene can potentially be used as a reinforcement MXene in alloys requiring even higher processing temperatures.

With about 30 MXene species currently available, mechanical and rheological properties of technologically relevant lightweight metal alloys can be controlled by designing specific metal matrix 2D carbide or nitride interfaces. Strong metal-MXene bonding is also required for creating MXene-metal electrical contacts for MXene antennas,[59] fibers in smart textiles,[60] battery and supercapacitor electrodes.[61] Brazing and soldering of MXenes require good wetting by metal and

high interfacial strength. Those applications will benefit from the data reported in this work, even though different metal alloys are used.

## METHODS

**MXene exfoliation *via* Minimally intensive layer delamination (MILD).** $Ti_3C_2T_x$ was synthesized using the published procedure.[21] The etching solution was prepared by dissolving 4.8 g of LiF in 60 ml of 9 M HCl under continuous stirring. 3 g of $Ti_3AlC_2$ MAX phase was added slowly (over the course of 5 min) to the etching solution. The mixture was stirred for 24 h at room temperature. The acidic mixture was further washed with 1.6 L of deionized $H_2O$ *via* centrifugation (5 min per cycle at 3260 g)/redispersion cycles. 270 ml of deionized $H_2O$ were then added and the solution was spun at 3260 g for 15 mins to separate the dark-green colloidal solution of delaminated $Ti_3C_2T_x$ sheets from the unetched $Ti_3AlC_2$ MAX phase and non-delaminated $Ti_3C_2T_x$ sheets (precipitate 1). The colloidal solution was decanted and 300 ml of deionized $H_2O$ were added followed by centrifugation for 1.5 h at 10543 g. Another 270 ml of deionized $H_2O$ were added to precipitate 1 to render more delaminated MXenes. The centrifugation/delamination cycles were repeated until further addition of deionized $H_2O$ to precipitate 1 did not result in dark green solution after 3260 g, 15 mins centrifugation. The collected precipitate containing delaminated MXenes was dried under vacuum for >12 h for further use. The typical yield of delaminated $Ti_3C_2T_x$ MXenes was 30-33 %.

**Intercalation with Tetramethylammonium hydroxide (TMAOH).** We noticed that the reported procedure of using 48 wt. % HF etching of $Ti_3AlC_2$ MAX phase followed by TMAOH intercalation of the multi-layer $Ti_3C_2T_x$ sheets was not effective in rendering sufficient yield of the delaminated MXene sheets. Hence TMAOH interaction was performed on MILD MXenes. Typically, ~1 g of MILD synthesized $Ti_3C_2T_x$ MXenes was stirred in 100 ml of 25 wt. % aqueous TMAOH solution for 24 h. The particles were then precipitated *via* centrifugation at 3260 g for 5 mins and 200 ml of deionized $H_2O$ was added. The solution was then ultrasonicated for 1.5 h while continuously bubbling Ar gas to avoid oxidation of flakes. $TMA^+$ intercalated $Ti_3C_2T_x$ sheets were then precipitated with MeOH/acetone mixture *via* centrifugation at 10543 g for 45 mins. This procedure results in almost quantitative yield of $TMA^+$ intercalated $Ti_3C_2T_x$ sheets. The collected precipitate

was dried at 120°C under vacuum to get rid of intercalated water before further use in the composite synthesis.

**Mg-Li alloy with $Ti_3C_2T_x$ MXenes.** All operations involving composite synthesis were performed in Ar filled glovebox with oxygen and moisture levels below 1 ppm. For ease of handling, Mg-Li alloy containing 60 at. % of Li (m.p. ~480 °C) was first prepared by melting Mg ingots (1.04 g) and Li pellets (445 mg) at 660 °C in a niobium crucible. 80-100 mg of $Ti_3C_2T_x$ MXene powder were infused into the melt at 530 °C with the assistance of probe sonication (Sonics Vibra Cell, VCX 750; 20 kHz, 105 μm amplitude, Ti-6Al-4V tip) for 2 mins. Once the required amount of MXenes had been introduced into the melt (~1.8 g), Mg ingots (1.37 g) were added at 700°C to the composite to dilute the concentration of Li (w.r.t. Mg) to 39 at. %. The resultant liquid metal alloy with MXenes was additionally ultrasound processed at 700 °C for 5 minutes to ensure complete mixing with the freshly introduced Mg metal. A typical MXene containing Mg-Li alloy composite was viscous enough so that it could be directly shaped while molten into an approximately rectangular shape (thixoforging technique) on a niobium substrate. The composite was allowed to cool down naturally to room temperature. Fabrication of Mg-Li MMC with $TiC_{0.9}$ NCs followed the same procedure as for the fabrication of Mg-Li alloy MMC with MXenes.

**Al doped Mg-Li alloy with $Ti_3C_2T_x$ MXenes.** In case of additional alloying with Al, the procedure was similar to Mg-Li alloy composite synthesis except that Al pellets were added into Mg-Li alloy (60 at. % of Li) at 530 °C before introducing MXenes.

**Ga liquid metal with $Ti_3C_2T_x$/$TMA^+$ MXenes.** 1.9 at. % of Mg (50 mg) was dissolved in liquid Ga (7.465 g) at 200 °C in a glass vial. The addition of the small amount of Mg was crucial for liquid Ga to wet MXenes (see Supporting Information for further discussion). $Ti_3C_2T_x$ MXene powder was infused into the alloy at 45 °C (to keep Ga fully molten) with the assistance of ultrasound (Sonics Vibra Cell, VCX 750, 20 kHz, 105 μm amplitude, Ti-6Al-4V tip). The gelated composite was transferred into an alumina crucible and additionally annealed at 700 °C for 30 mins to mimic the high temperature processing conditions in Mg-Li alloy.

**Rheology measurements.** Rheology measurements were performed on an Anton Paar MCR 301 rheometer equipped with a Peltier temperature control system. Measurements were taken in

parallel plate geometry, using a 25 mm-diameter tool. The temperature was maintained at 45 $^{0}$C. Please refer to the supporting information for further details on the measurement protocol.

**Mechanical testing.** Samples were machined into rectangular pillars with aspect ratio between 1:2 and 1:3. The compressive tests were performed on an Instron 5800 series materials tester using a 50 kN load cell at a strain rate of $10^{-3}$ $s^{-1}$. At least three replicate samples were tested for each composite. Vickers hardness tests were conducted on a Duramin 5 hardness tester using 0.98 N load for 5 s. Indentation was performed at least 17 times on the same sample to determine the average HV value and its standard deviation.

**Synchrotron X-ray diffraction (XRD).** The high-resolution synchrotron XRD data were collected using mail-in program available at 11-BM beamline at the Advanced Photon Source (APS) at Argonne National Laboratory with the X-ray wavelength of 0.412779 Å and 0.001° 2θ binning. Data were subsequently re-binned using a coarser spacing of 0.01° 2θ in order to facilitate convergence of the Rietveld refinements. All samples were sealed in Kapton capillaries (0.8 mm inner diameter) with epoxy. The capillaries were spun at 60 Hz during the measurement to maximize random orientation of the powders. The samples were measured for 60 minutes each.

**Transmission electron microscopy (TEM).** The TEM images were obtained using a 300 kV FEI Tecnai F30 microscope. Samples for TEM were prepared by dropcasting a dilute sample of MXene solution onto a lacey carbon grid from Ted Pella. The MMC samples for TEM were prepared using FIB-SEM.

**Focused Ion Beam-Scanning Electron Microscopy (FIB-SEM).** Thin samples of MMCs for TEM analysis were prepared in a TESCAN LYRA3 field-emission scanning electron microscope equipped with a Cobra liquid metal ion gun for focused ion beam operation and two X-Max-80 silicon drift x-detectors (SDD) for energy dispersive X-ray (EDX) analysis. A thin lamellar was first lifted out of the bulk MMC sample and mounted onto a TEM half-grid using E-beam deposited Pt. The attached lamellar was further thinned to ~100 nm using 30 kV (voltage), 150-500 pA (current) FIB.

## ASSOCIATED CONTENT

### Supporting Information

Additional experimental details, fitting of XPS spectra, details of Rietveld refinement and Estimation of van der Waals potentials. This material is available free of charge *via* the Internet at http://.

The authors declare no competing financial interests.

## AUTHOR INFORMATION

### Corresponding Author

dvtalapin@uchicago.edu

## ACKNOWELDGEMENTS

We thank Dr. Himchan Cho for assistance with AFM measurements. We also thank Margaret Hudson for helpful discussions and critical review of the manuscript. This work was supported by the National Science Foundation under award number DMR-1611371, by the Department of Defense (DOD) Air Force Office of Scientific Research under grant number FA9550-18-1-0099, and by University of Chicago Materials Research Science and Engineering Center, which is funded by NSF under award number DMR-1420709. We acknowledge the use of 11-BM high resolution powder XRD facility at the Argonne National Laboratory. Use of the Advanced Photon Source at Argonne National Laboratory was supported by the U. S. Department of Energy, Office of Science, Office of Basic Energy Sciences, under Contract No. DE-AC02-06CH11357. Work at Drexel University was also supported by MuRata Manufacturing Co., Ltd., Japan.

## REFERENCES

(1) Begley, M. R.; Gianola, D. S.; Ray, T. R., Bridging Functional Nanocomposites to Robust Macroscale Devices. *Science* **2019,** *364*, eaav4299.

(2) Llordés, A.; Garcia, G.; Gazquez, J.; Milliron, D. J., Tunable Near-Infrared and Visible-Light Transmittance in Nanocrystal-in-Glass Composites. *Nature* **2013,** *500*, 323.

(3) Shahzad, F.; Alhabeb, M.; Hatter, C. B.; Anasori, B.; Man Hong, S.; Koo, C. M.; Gogotsi, Y., Electromagnetic Interference Shielding with 2D Transition Metal Carbides (MXenes). *Science* **2016,** *353*, 1137-1140.

(4) Luo, S.; Yu, J.; Yu, S.; Sun, R.; Cao, L.; Liao, W.-H.; Wong, C.-P., Significantly Enhanced Electrostatic Energy Storage Performance of Flexible Polymer Composites by Introducing Highly Insulating-Ferroelectric Microhybrids as Fillers. *Adv. Energy Mater.* **2019,** *9*, 1803204.

(5) Casati, R.; Vedani, M., Metal Matrix Composites Reinforced by Nano-Particles—a Review. *Metals* **2014,** *4*, 65.

(6) Kollo, L.; Leparoux, M.; Bradbury, C. R.; Jäggi, C.; Carreño-Morelli, E.; Rodríguez-Arbaizar, M., Investigation of Planetary Milling for Nano-Silicon Carbide Reinforced Aluminium Metal Matrix Composites. *J. Alloys Compd.* **2010,** *489*, 394-400.

(7) Thakur, S. K.; Srivatsan, T. S.; Gupta, M., Synthesis and Mechanical Behavior of Carbon Nanotube–Magnesium Composites Hybridized with Nanoparticles of Alumina. *Mater. Sci. Eng., A* **2007,** *466*, 32-37.

(8) Nieto, A.; Bisht, A.; Lahiri, D.; Zhang, C.; Agarwal, A., Graphene Reinforced Metal and Ceramic Matrix Composites: A Review. *Int. Mater. Rev.* **2017,** *62*, 241-302.

(9) Esawi, A. M. K.; Morsi, K.; Sayed, A.; Gawad, A. A.; Borah, P., Fabrication and Properties of Dispersed Carbon Nanotube–Aluminum Composites. *Mater. Sci. Eng., A* **2009,** *508*, 167-173.

(10) Chen, L.-Y.; Xu, J.-Q.; Choi, H.; Pozuelo, M.; Ma, X.; Bhowmick, S.; Yang, J.-M.; Mathaudhu, S.; Li, X.-C., Processing and Properties of Magnesium Containing a Dense Uniform Dispersion of Nanoparticles. *Nature* **2015,** *528*, 539.

(11) Kok, M., Production and Mechanical Properties of $Al_2O_3$ Particle-Reinforced 2024 Aluminium Alloy Composites. *J. Mater. Process. Technol.* **2005,** *161*, 381-387.

(12) Dorri Moghadam, A.; Omrani, E.; Menezes, P. L.; Rohatgi, P. K., Mechanical and Tribological Properties of Self-Lubricating Metal Matrix Nanocomposites Reinforced by Carbon Nanotubes (CNTs) and Graphene – a Review. *Composites, Part B* **2015,** *77*, 402-420.

(13) Cook, W. H. *Corrosion Reisistance of Various Ceramics and Cermets to Liquid Metals*; Oak Ridge National Lab: Oak Ridge, TN, 1960.

(14) Wu, R.; Yan, Y.; Wang, G.; Murr, L. E.; Han, W.; Zhang, Z.; Zhang, M., Recent Progress in Magnesium–Lithium Alloys. *Int. Mater. Rev.* **2015,** *60*, 65-100.

(15) Naguib, M.; Kurtoglu, M.; Presser, V.; Lu, J.; Niu, J.; Heon, M.; Hultman, L.; Gogotsi, Y.; Barsoum, M. W., Two-Dimensional Nanocrystals Produced by Exfoliation of $Ti_3AlC_2$. *Adv. Mater.* **2011,** *23*, 4248-4253.

(16) Anasori, B.; Lukatskaya, M. R.; Gogotsi, Y., 2D Metal Carbides and Nitrides (MXenes) for Energy Storage. *Nat. Rev. Mater.* **2017,** *2*, 16098.

(17) Lipatov, A.; Lu, H.; Alhabeb, M.; Anasori, B.; Gruverman, A.; Gogotsi, Y.; Sinitskii, A., Elastic Properties of 2D $Ti_3C_2T_x$ MXene Monolayers and Bilayers. *Sci. Adv.* **2018,** *4*, eaat0491.

(18) Borysiuk, V. N.; Mochalin, V. N.; Gogotsi, Y., Bending Rigidity of Two-Dimensional Titanium Carbide (MXene) Nanoribbons: A Molecular Dynamics Study. *Comput. Mater. Sci.* **2018,** *143*, 418-424.

(19) Nicklow, R.; Wakabayashi, N.; Smith, H. G., Lattice Dynamics of Pyrolytic Graphite. *Phys. Rev. B* **1972,** *5*, 4951-4962.

(20) Xu, W.; Birbilis, N.; Sha, G.; Wang, Y.; Daniels, J. E.; Xiao, Y.; Ferry, M., A High-Specific-Strength and Corrosion-Resistant Magnesium Alloy. *Nat. Mater.* **2015,** *14*, 1229.

(21) Alhabeb, M.; Maleski, K.; Anasori, B.; Lelyukh, P.; Clark, L.; Sin, S.; Gogotsi, Y., Guidelines for Synthesis and Processing of Two-Dimensional Titanium Carbide ($Ti_3C_2T_x$ MXene). *Chem. Mater.* **2017,** *29*, 7633-7644.

(22) Wang, Z.; Xuan, J.; Zhao, Z.; Li, Q.; Geng, F., Versatile Cutting Method for Producing Fluorescent Ultrasmall Mxene Sheets. *ACS Nano* **2017,** *11*, 11559-11565.

(23) Seredych, M.; Shuck, C. E.; Pinto, D.; Alhabeb, M.; Precetti, E.; Deysher, G.; Anasori, B.; Kurra, N.; Gogotsi, Y., High-Temperature Behavior and Surface Chemistry of Carbide MXenes Studied by Thermal Analysis. *Chem. Mater.* **2019**.

(24) Ibrahim, I. A.; Mohamed, F. A.; Lavernia, E. J., Particulate Reinforced Metal Matrix Composites — a Review. *J. Mater. Sci.* **1991,** *26*, 1137-1156.

(25) Daeneke, T.; Khoshmanesh, K.; Mahmood, N.; de Castro, I. A.; Esrafilzadeh, D.; Barrow, S. J.; Dickey, M. D.; Kalantar-zadeh, K., Liquid Metals: Fundamentals and Applications in Chemistry. *Chem. Soc. Rev.* **2018,** *47*, 4073-4111.

(26) Dezellus, O.; Eustathopoulos, N., Fundamental Issues of Reactive Wetting by Liquid Metals. *J. Mater. Sci.* **2010,** *45*, 4256-4264.

(27) Dudiy, S. V.; Lundqvist, B. I., Wetting of TiC and TiN by Metals. *Phys. Rev. B* **2004,** *69*, 125421.

(28) Israelachvili, J. N., *Intermolecular and Surface Forces*. Academic Press: London, 2011.

(29) Kamysbayev, V.; Srivastava, V.; Ludwig, N. B.; Borkiewicz, O. J.; Zhang, H.; Ilavsky, J.; Lee, B.; Chapman, K. W.; Vaikuntanathan, S.; Talapin, D. V., Nanocrystals in Molten Salts and Ionic Liquids: Experimental Observation of Ionic Correlations Extending Beyond the Debye Length. *ACS Nano* **2019**, *13*, 5760-5770.

(30) Oh, S. H.; Kauffmann, Y.; Scheu, C.; Kaplan, W. D.; Rühle, M., Ordered Liquid Aluminum at the Interface with Sapphire. *Science* **2005,** *310*, 661-663.

(31) Reichert, H.; Klein, O.; Dosch, H.; Denk, M.; Honkimäki, V.; Lippmann, T.; Reiter, G., Observation of Five-Fold Local Symmetry in Liquid Lead. *Nature* **2000,** *408*, 839-841.

(32) Huisman, W. J.; Peters, J. F.; Zwanenburg, M. J.; de Vries, S. A.; Derry, T. E.; Abernathy, D.; van der Veen, J. F., Layering of a Liquid Metal in Contact with a Hard Wall. *Nature* **1997,** *390*, 379-381.

(33) Zhang, H.; Dasbiswas, K.; Ludwig, N. B.; Han, G.; Lee, B.; Vaikuntanathan, S.; Talapin, D. V., Stable Colloids in Molten Inorganic Salts. *Nature* **2017,** *542*, 328.

(34) Parsegian, V. A., *Van Der Waals Forces: A Handbook for Biologists, Chemists, Engineers, and Physicists*. Cambridge University Press: Cambridge, 2005.

(35) Dillon, A. D.; Ghidiu, M. J.; Krick, A. L.; Griggs, J.; May, S. J.; Gogotsi, Y.; Barsoum, M. W.; Fafarman, A. T., Highly Conductive Optical Quality Solution-Processed Films of 2D Titanium Carbide. *Adv. Funct. Mater.* **2016,** *26*, 4162-4168.

(36) Xu, J. Q.; Chen, L. Y.; Choi, H.; Li, X. C., Theoretical Study and Pathways for Nanoparticle Capture During Solidification of Metal Melt. *J. Phys.: Condens. Matter* **2012,** *24*, 255304.

(37) Berdiyorov, G. R., Optical Properties of Functionalized $Ti_3C_2T_2$ (T = F, O, OH) MXene: First-Principles Calculations. *AIP Adv.* **2016,** *6*, 055105.

(38) Trappe, V.; Prasad, V.; Cipelletti, L.; Segre, P. N.; Weitz, D. A., Jamming Phase Diagram for Attractive Particles. *Nature* **2001,** *411*, 772.

(39) Eberle, A. P. R.; Wagner, N. J.; Castañeda-Priego, R., Dynamical Arrest Transition in Nanoparticle Dispersions with Short-Range Interactions. *Phys. Rev. Lett.* **2011,** *106*, 105704.

(40) Tsurusawa, H.; Leocmach, M.; Russo, J.; Tanaka, H., Direct Link between Mechanical Stability in Gels and Percolation of Isostatic Particles. *Sci. Adv.* **2019,** *5*, eaav6090.

(41) Keene, B. J., Review of Data for the Surface Tension of Pure Metals. *Int. Mater. Rev.* **1993,** *38*, 157-192.

(42) Mason, T. G.; Weitz, D. A., Linear Viscoelasticity of Colloidal Hard Sphere Suspensions near the Glass Transition. *Phys. Rev. Lett.* **1995,** *75*, 2770-2773.

(43) Gisler, T.; Ball, R. C.; Weitz, D. A., Strain Hardening of Fractal Colloidal Gels. *Phys. Rev. Lett.* **1999,** *82*, 1064-1067.

(44) Moller, P.; Fall, A.; Chikkadi, V.; Derks, D.; Bonn, D., An Attempt to Categorize Yield Stress Fluid Behaviour. *Philos. Trans. R. Soc., A* **2009,** *367*, 5139-5155.

(45) Fan, Z., Semisolid Metal Processing. *Int. Mater. Rev.* **2002,** *47*, 49-85.

(46) Chen, W.; Thornley, L.; Coe, H. G.; Tonneslan, S. J.; Vericella, J. J.; Zhu, C.; Duoss, E. B.; Hunt, R. M.; Wight, M. J.; Apelian, D.; Pascall, A. J.; Kuntz, J. D.; Spadaccini, C. M., Direct Metal Writing: Controlling the Rheology through Microstructure. *Appl. Phys. Lett.* **2017,** *110*, 094104.

(47) Sang, X.; Xie, Y.; Yilmaz, D. E.; Lotfi, R.; Alhabeb, M.; Ostadhossein, A.; Anasori, B.; Sun, W.; Li, X.; Xiao, K.; Kent, P. R. C.; van Duin, A. C. T.; Gogotsi, Y.; Unocic, R. R., *In Situ* Atomistic Insight into the Growth Mechanisms of Single Layer 2D Transition Metal Carbides. *Nat. Commun.* **2018,** *9*, 2266.

(48) Ghidiu, M.; Barsoum, M. W., The {110} Reflection in X-Ray Diffraction of MXene Films: Misinterpretation and Measurement *via* Non-Standard Orientation. *J. Am. Ceram. Soc.* **2017,** *100*, 5395-5399.

(49) Tang, S.; Xin, T.; Xu, W.; Miskovic, D.; Sha, G.; Quadir, Z.; Ringer, S.; Nomoto, K.; Birbilis, N.; Ferry, M., Precipitation Strengthening in an Ultralight Magnesium Alloy. *Nat. Commun.* **2019,** *10*, 1003.

(50) Aroyo Mois, I.; Perez-Mato Juan, M.; Capillas, C.; Kroumova, E.; Ivantchev, S.; Madariaga, G.; Kirov, A.; Wondratschek, H., Bilbao Crystallographic Server: I. Databases and Crystallographic Computing Programs. In *Zeitschrift für Kristallographie - Crystalline Materials*, 2006; Vol. 221, p 15.

(51) Fu, Z. H.; Zhang, Q. F.; Legut, D.; Si, C.; Germann, T. C.; Lookman, T.; Du, S. Y.; Francisco, J. S.; Zhang, R. F., Stabilization and Strengthening Effects of Functional Groups in Two-Dimensional Titanium Carbide. *Phys. Rev. B* **2016,** *94*, 104103.

(52) Bauer, E.; van der Merwe, J. H., Structure and Growth of Crystalline Superlattices: From Monolayer to Superlattice. *Phys. Rev. B* **1986,** *33*, 3657-3671.

(53) Siegel, D. J.; Hector, L. G.; Adams, J. B., *Ab Initio* Study of Al-Ceramic Interfacial Adhesion. *Phys. Rev. B* **2003,** *67*, 092105.

(54) Bianchi, E.; Largo, J.; Tartaglia, P.; Zaccarelli, E.; Sciortino, F., Phase Diagram of Patchy Colloids: Towards Empty Liquids. *Phys. Rev. Lett.* **2006,** *97*, 168301.

(55) Yu, Z.; Tang, A.; Wang, Q.; Gao, Z.; He, J.; She, J.; Song, K.; Pan, F., High Strength and Superior Ductility of an Ultra-Fine Grained Magnesium–Manganese Alloy. *Mater. Sci. Eng., A* **2015,** *648*, 202-207.

(56) Kawamori, S.; Machida, T., Microstructure and Mechanical Properties of Alumina-Dispersed Magnesium Fabricated Using Mechanical Alloying Method. *Mater. Trans.* **2007,** *48*, 373-379.

(57) Anasori, B.; Caspi, E. a. N.; Barsoum, M. W., Fabrication and Mechanical Properties of Pressureless Melt Infiltrated Magnesium Alloy Composites Reinforced with TiC and $Ti_2AlC$ Particles. *Mater. Sci. Eng., A* **2014,** *618*, 511-522.

(58) Zhou, J.; Zha, X.; Chen, F. Y.; Ye, Q.; Eklund, P.; Du, S.; Huang, Q., A Two-Dimensional Zirconium Carbide by Selective Etching of $Al_3C_3$ from Nanolaminated $Zr_3Al_3C_5$. *Angew. Chem.* **2016,** *128*, 5092-5097.

(59) Sarycheva, A.; Polemi, A.; Liu, Y.; Dandekar, K.; Anasori, B.; Gogotsi, Y., 2D Titanium Carbide (MXene) for Wireless Communication. *Sci. Adv.* **2018,** *4*, eaau0920.

(60) Wang, Q.-W.; Zhang, H.-B.; Liu, J.; Zhao, S.; Xie, X.; Liu, L.; Yang, R.; Koratkar, N.; Yu, Z.-Z., Multifunctional and Water-Resistant MXene-Decorated Polyester Textiles with Outstanding Electromagnetic Interference Shielding and Joule Heating Performances. *Adv. Funct. Mater.* **2019,** *29*, 1806819.

(61) Xia, Y.; Mathis, T. S.; Zhao, M.-Q.; Anasori, B.; Dang, A.; Zhou, Z.; Cho, H.; Gogotsi, Y.; Yang, S., Thickness-Independent Capacitance of Vertically Aligned Liquid-Crystalline MXenes. *Nature* **2018,** *557*, 409-412.

## TOC Graphic

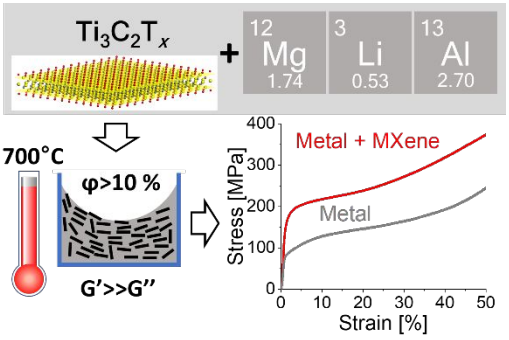
$Ti_3C_2T_x$
+
12
Mg
1.74
3
Li
0.53
13
Al
2.70
700°C
φ>10 %
G'>>G''
Metal + MXene
Metal
Stress [MPa]
Strain [%]
0
100
200
300
400
0
10
20
30
40
50